GDCh

Research Articles

Angewandte
Chemie
International Edition
www.angewandte.org

VIP **CO₂ Reduction** *Very Important Paper*

Microwave-Assisted Rapid Synthesis of MOF-Based Single-Atom Ni Catalyst for CO₂ Electroreduction at Ampere-Level Current

Ming Wen, Nana Sun, Long Jiao,* Shuang-Quan Zang,* and Hai-Long Jiang*

Abstract: Carbon-based single-atom catalysts (SACs) have attracted tremendous interest in heterogeneous catalysis. However, the common electric heating techniques to produce carbon-based SACs usually suffer from prolonged heating time and tedious operations. Herein, a general and facile microwave-assisted rapid pyrolysis method is developed to afford carbon-based SACs within 3 min without inert gas protection. The obtained carbon-based SACs present high porosity and comparable carbonization degree to those obtained by electric heating techniques. Specifically, the single-atom Ni implanted N-doped carbon (Ni₁–N–C) derived from a Ni-doped metal–organic framework (Ni-ZIF-8) exhibits remarkable CO Faradaic efficiency (96%) with a substantial CO partial current density (j_{CO}) up to 1.06 A/cm² in CO₂ electroreduction, far superior to the counterpart obtained by traditional pyrolysis with electric heating. Mechanism investigations reveal that the resulting Ni₁–N–C presents abundant defective sites and mesoporous structure, greatly facilitating CO₂ adsorption and mass transfer. This work establishes a versatile approach to rapid and large-scale synthesis of SACs as well as other carbon-based materials for efficient catalysis.

Introduction

Single-atom catalysts (SACs), with maximized metal atom utilization and unique geometric/electronic structures, have recently garnered significant attention and become a hotspot in the field of catalysis.[1] Among various supports for SACs,

porous carbon materials have been widely employed as ideal candidates due to their large surface areas, outstanding electronic conductivity, easy tailorability, and high stability.[2,3] Generally, SACs with carbon as supports are extensively obtained through the pyrolysis of organic precursors containing targeted metal species in conventional electric heating equipment, mainly tubular furnaces, at temperatures above 700°C.[3] Unfortunately, such a furnace annealing process usually requires long heating time (several hours), high energy input and inert gas protection, which significantly lowers the time and energy efficiency.[3e,4] In fact, the prolonged thermal treatment readily induces migration and aggregation of metal atoms, bringing challenges to the fabrication of SACs.[5] It is expected to develop more efficient and easily manageable carbonization methods with reduced time and energy.

Microwave heating, an alternative heating technology, has gained widespread usage in recent years.[6–9] In stark contrast with the conventional electric heating technique that relies on an inefficient heat conduction process (from equipment to the sample), microwaves can be adsorbed by the samples directly and converted into heat via dipole rotation and ionic conduction mechanisms.[7a] In view of the distinct heating principles, microwave-assisted heating enables rapid heating within a short period (several seconds/minutes),[7b,c] which would effectively inhibit the migration and aggregation of metal atoms during SACs preparation. Unfortunately, due to the poor microwave adsorption ability of most organic precursors,[8] the carbonization of organic precursors by microwave-assisted heating to fabricate carbon-based SACs remains an uncultivated land. The introduction of external microwave absorptive media would effectively address the issue above,[9] offering a promising strategy for the application of microwave heating technology in the synthesis of carbon-based SACs.

In addition to the elaborate selection of heating techniques, the choice of suitable precursors is also crucial as it could significantly influence the microstructure and physicochemical properties of the resulting SACs. Metal–organic frameworks (MOFs),[10] a class of crystalline porous materials, have gained widespread attentions in catalysis due to their ultrahigh surface area, excellent structural adaptability, and diverse compositions.[11] During pyrolysis, their structural and compositional advantages can be largely inherited to the carbon-based materials, making MOFs ideal precursors for the fabrication of carbon-based SACs.[10d,11c,12] The combination of microwave heating technology (time/energy saving and ease of handling) with MOF precursors (high porosity, accurate designability and flexible tailorabil-

[*] Dr. M. Wen, Prof. Dr. S.-Q. Zang
Henan Key Laboratory of Crystalline Molecular Functional Materials, Henan International Joint Laboratory of Tumor Theranostical Cluster Materials, Green Catalysis Center, and College of Chemistry, Zhengzhou University, Zhengzhou, Henan 450001, P. R. China
E-mail: zangsqzg@zzu.edu.cn

Dr. M. Wen, Dr. N. Sun, Prof. Dr. L. Jiao, Prof. Dr. H.-L. Jiang
Hefei National Research Center for Physical Sciences at the Microscale, Department of Chemistry, University of Science and Technology of China, Hefei, Anhui 230026, P. R. China
E-mail: longjiao@ustc.edu.cn
jianglab@ustc.edu.cn

Prof. Dr. L. Jiao, Prof. Dr. H.-L. Jiang
Institute of Energy, Hefei Comprehensive National Science Center, Hefei, Anhui 230031, P. R. China

ity) should be an ideal strategy for the construction of carbon-based SACs.

Based on the aforementioned considerations, a facile and universal microwave-assisted rapid pyrolysis method has been developed with the assistance of $ZnCl_2/KCl$ mixture as microwave absorber. By adopting Ni-doped zeolite imidazole framework-8 (Ni-ZIF-8) as the precursor, single-atom Ni implanted N-doped carbon (Ni_1–N–C) is obtained in 3 min only, in the absence of inert gas protection (Scheme 1). The optimized Ni_1–N–C catalyst exhibits an ultrahigh CO partial current density (j_{CO}; 1.06 A/cm^2) with CO Faradaic efficiency (FE_{CO}) up to 96 % in electrochemical CO_2 reduction. This performance is far superior to that of the Ni_1–N–C-furnace catalyst obtained via traditional electric heating in furnace. Results reveal that the rapid synthesis of Ni_1–N–C assisted by $ZnCl_2/KCl$ favors the formation of abundant defective sites and the mesoporous structure. This greatly facilitates the adsorption of CO_2 and accelerates mass transfer, thereby improving the performance toward CO_2 electroreduction. Furthermore, such microwave-induced pyrolysis strategy can be extended to construct carbon-based SACs containing different metal species from various precursors, highlighting its great potential for the general synthesis of SACs in practical production.
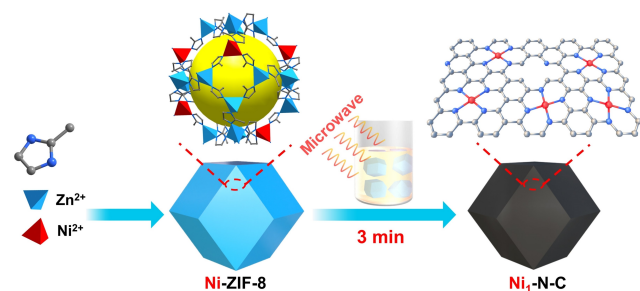
Scheme 1. Illustration showing the fabrication of Ni_1–N–C by microwave-assisted rapid pyrolysis.
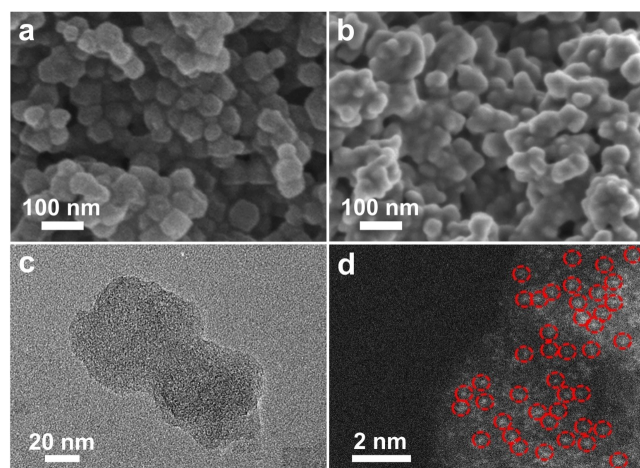
Figure 1. SEM images of a) Ni-ZIF-8 and b) Ni_1–N–C-50. c) TEM and d) the aberration-corrected HAADF-STEM images of Ni_1–N–C-50.

Results and Discussion

By the solvothermal reaction of Zn^{2+}, Ni^{2+}, and 2-methylimidazole, Ni-doped ZIF-8 (Ni-ZIF-8) with an identical crystalline structure and morphology to the pristine ZIF-8 has been constructed successfully (Figure 1a, S1 and S2).[13] Unfortunately, when Ni-ZIF-8 alone is exposed to microwave radiation, no thermal effect can be induced due to the microwave transparency property of Ni-ZIF-8, and therefore the crystal structure of Ni-ZIF-8 is well retained (Figure S2). To enhance the microwave absorption ability, $ZnCl_2$, a polar compound with strong microwave absorption capacity,[9a,14] is selected as the microwave absorber to mix with Ni-ZIF-8. To our delight, the mixture of Ni-ZIF-8 and $ZnCl_2$ presents obvious microwave absorption and Ni-ZIF-8 is successfully carbonized within 3 min, affording Ni–N–C–$ZnCl_2$ material (Figure S3). Thanks to the low melting point of $ZnCl_2$ (283 °C), fluid molten $ZnCl_2$ is readily formed before the carbonization of Ni-ZIF-8, providing the isolation effect surrounding Ni-ZIF-8 particles to prevent oxygen penetration. Therefore, the carbonization of Ni-ZIF-8 can be achieved directly in air without the protection of inert gases, much easier to handle than the traditional electric heating process. Unfortunately, as revealed by Raman and X-ray diffraction (XRD) characterizations, the carbonization degree of Ni–N–C–$ZnCl_2$ is insufficient (Figure S4), reflecting the relatively low carbonization temperature induced by $ZnCl_2$.

To further improve the carbonization temperature, KCl is introduced as a promoter and mixed with $ZnCl_2$ to enhance the microwave absorption capacity. On the one hand, the mixture of $ZnCl_2$–KCl presents a much lower melting point than pure $ZnCl_2$ or KCl as indicated by the binary phase diagram of $ZnCl_2$–KCl,[15a] and the molten state of $ZnCl_2$/KCl mixture formed at lower temperature will further boost the microwave absorption ability due to the occurrence of the ionic conduction mechanism in molten state.[15b] On the other hand, the introduced KCl, although not a good absorber, can further improve the ion conductivity of the molten $ZnCl_2$–KCl system, which greatly enhances microwave absorption and induces a higher heating temperature compared with pure $ZnCl_2$.[15c] This is well supported by the significantly rising temperature observed for the $ZnCl_2$/KCl/Ni-ZIF-8 mixture along with the increase of KCl amount (Figure S5). To further prove the critical role of the enhanced ion conductivity brought by KCl on improving microwave absorption, other ionic compounds featuring high ion conductivity, such as LiCl and NaCl, are also adopted to substitute KCl in the $ZnCl_2$–KCl system. Results show that both $ZnCl_2$–LiCl and $ZnCl_2$–NaCl systems present comparable heating temperatures to $ZnCl_2$–KCl (Figure S6). In contrast, $AlCl_3$, a covalent compound with low ion conductivity, is not favorable to microwave absorption and the $ZnCl_2$–$AlCl_3$ mixture gives low heating temperature similar to pure $ZnCl_2$ (Figure S5 and S6), illustrating the significance of ion conductivity for boosting microwave absorption ability.

Based on the results above, a series of Ni_1–N–C–X catalysts (X = 15, 50 and 100, corresponding to KCl/Ni-ZIF-

8 mass ratios of 0.15, 0.50 and 1.00, respectively) can be obtained successfully via microwave irradiation within 3 min. The XRD patterns of the resulting samples suggest an increase in carbon peak intensities along with increased KCl amount, revealing an elevated carbonization temperature from Ni_1–N–C-15 to Ni_1–N–C-100 (Figure S7). Meanwhile, no metallic phases can be found in the XRD patterns, which excludes the formation of large Ni particles and indicates the possible existence of atomically dispersed Ni or tiny Ni aggregates (Figure S7). Raman spectra suggest that the Ni_1–N–C–X (X=15, 50 and 100) series possess comparable carbonization degree to the Ni_1–N–C-furnace prepared by conventional electric heating in furnace (900 °C for 2 h in N_2) (Figure S4 and Table S1). Moreover, the gradually increased I_D/I_G values from Ni_1–N–C-15 to Ni_1–N–C-100 suggest that more carbon defects are formed with the increase of KCl, reflecting the activation effect of K ions during the rapid carbonization process (Figure S4).[16]

The SEM images of Ni_1–N–C–X (X=15, 50 and 100) present the well-retained morphology of Ni-ZIF-8 after microwave-assisted pyrolysis (Figure 1b, S8a and S8b). No Ni particles can be observed from the TEM images of Ni_1–N–C–X (X=15, 50, and 100), in accordance with the XRD analysis (Figure 1c, S7, S8d and S8e). Inductively coupled plasma atomic emission spectrometry (ICP-AES) and elemental analysis indicate similar Ni contents (in the range of 1.3–1.6 wt%) and high N contents (in the range of 6.7–8.6%) in Ni_1–N–C–X (X=15, 50, and 100) (Table S2 and S3). Besides, the N contents of Ni_1–N–C-50 and Ni_1–N–C-100 are lower than Ni_1–N–C-15, further revealing the higher pyrolysis temperature of Ni_1–N–C-50 and Ni_1–N–C-100 (Table S3). The N_2 sorption isotherms present moderately high surface areas of Ni_1–N–C-15 (154 m^2/g), Ni_1–N–C-50 (737 m^2/g), and Ni_1–N–C-100 (878 m^2/g) (Figure S9 and Table S1). In addition, prominent mesoporous structures can be observed in Ni_1–N–C-50 and Ni_1–N–C-100 while Ni_1–N–C-15 shows little mesoporous feature, hinting the improved active site accessibility and mass transfer of Ni_1–N–C-50 and Ni_1–N–C-100 (Figure S9). Furthermore, taking Ni_1–N–C-50 as an example, the aberration-corrected high-angle annular dark-field scanning transmission electron microscopy (HAADF-STEM) observation clearly displays the atomic dispersion of Ni atoms (marked with red circles) (Figure 1d).

X-ray photoelectron spectroscopy (XPS) has been further employed to investigate the chemical compositions and electronic structures of different samples. The N 1s spectra of Ni_1–N–C-15, Ni_1–N–C-50 and Ni_1–N–C-100 indicate the existence of metal-N species (399.9 eV), which confirms the involvement of Ni–N coordination (Figure S10). Moreover, Ni 2p XPS spectra show that the Ni $2p_{3/2}$ binding energies of Ni_1–N–C–X (X=15, 50 and 100) are all located between Ni^0 (853.5 eV) and Ni^{2+} (856.0 eV), suggesting the positive valence state of Ni in Ni_1–N–C–X (Figure 2a).[12g,17a,b] Moreover, the binding energy of Ni in Ni_1–N–C-50 and Ni_1–N–C-100 are lower than Ni_1–N–C-15 (Figure 2a), manifesting the lower oxidation state of Ni species in Ni_1–N–C-50 and Ni_1–N–C-100 possibly due to higher temperatures generated in their synthesis. Since single-atom Ni sites at lower valence
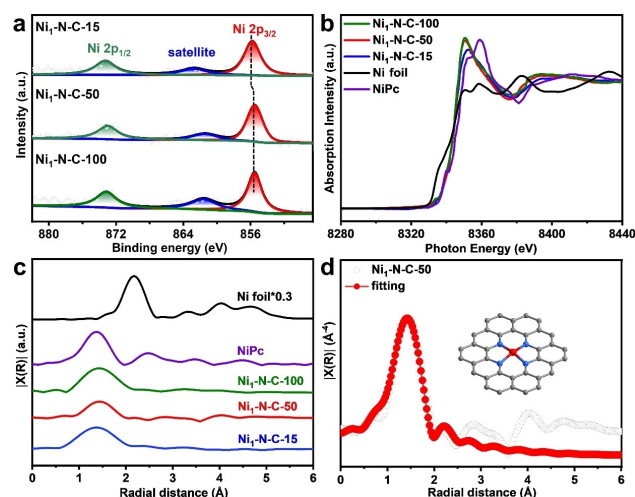

Figure 2. a) The Ni 2p XPS spectra of Ni_1–N–C-15, Ni_1–N–C-50 and Ni_1–N–C-100. b) The Ni K-edge XANES spectra and c) FT-EXAFS spectra of Ni_1–N–C-15, Ni_1–N–C-50, Ni_1–N–C-100, Ni foil and nickel phthalocyanine (simply as NiPc). d) EXAFS fitting of Ni_1–N–C-50 (inset: optimized coordination environment of Ni atoms).

state have been widely proved to be more favorable for CO_2 electroreduction,[12g,17a] the XPS analysis further indicates the better electrochemical performances of Ni_1–N–C-50 and Ni_1–N–C-100 to Ni_1–N–C-15 (Figure 2a). To further unravel the chemical environments of single metal atoms, X-ray absorption spectroscopy (XAS) analysis has been performed. The Ni K-edge X-ray absorption near-edge structure (XANES) spectra of Ni_1–N–C–X (X=15, 50 and 100) show the adsorption edge located between Ni foil and NiPc, indicating the positive valence state of $Ni^{\delta+}$ $(0<\delta<2)$ (Figure 2b). The Fourier transform-extended X-ray absorption fine structure (FT-EXAFS) spectra of Ni_1–N–C–X (X=15, 50 and 100) all showcase dominated peaks around 1.4 Å assigned to Ni–N bonding and no Ni–Ni scattering path is observed, further confirming the atomic dispersion of Ni (Figure 2c). The fitting results for FT-EXAFS spectra show that each Ni atom in Ni_1–N–C–X (X=15, 50 and 100) is coordinated with four N atoms in the form of Ni–N_4 configuration (Figure 2d, S11a and S11b, Table S4). As a control, Ni_1–N–C-furnace prepared by conventional furnace pyrolysis method has also been characterized. The XAS and TEM together with XRD analyses indicate the atomic dispersion of Ni in Ni_1–N–C-furnace without metal clusters or nanoparticles (Figure S7, S8c, S8f, S11c and S11d). Similar morphology and Ni contents as well as comparable carbonization degrees are also observed between Ni_1–N–C-furnace and Ni_1–N–C–X (X=15, 50, and 100) (Figure S4 and S8, Table S1 and S2). The biggest difference is that Ni_1–N–C-furnace presents a microporous feature in stark contrast with the abundant mesoporous feature of Ni_1–N–C-50 and Ni_1–N–C-100, demonstrating the superiority of the microwave-assisted pyrolysis for creating mesopores (Figure S9).

Inspired by the results above, electrochemical CO_2 reduction over the aforementioned catalysts has been

conducted. From linear scanning voltammetry (LSV) curves, it can be seen that the current densities of Ni_1–N–C–X (X = 15, 50 and 100) in CO_2-saturated electrolytes are much higher than those in N_2, implying their catalytic activity for CO_2 reduction (Figure S12–S14). In contrast, Ni–N–C–$ZnCl_2$ shows a weak current response for CO_2 reduction (Figure S15). Remarkably, Ni_1–N–C-50 and Ni_1–N–C-100 present much higher current responses and better FE_{CO} than Ni–N–C–$ZnCl_2$ and Ni_1–N–C-15 in CO_2-saturated electrolytes, manifesting their better CO_2 reduction performances (Figure 3a and 3b). In addition, H_2 is the only byproduct (no detectable liquid product) and its production is largely inhibited for Ni_1–N–C-50 and Ni_1–N–C-100 (Figure S16 and S17). Meanwhile, Ni_1–N–C-50 achieves superior CO partial current density (j_{CO}) compared with Ni_1–N–C-15 and Ni_1–N–C-100, manifesting that Ni_1–N–C-50 is the optimized catalyst (Figure S18). For comparison, N–C-50 without Ni has been further prepared and shows much lower FE_{CO} than Ni_1–N–C-50, indicating that the single Ni atoms are the real active sites (Figure S19). To further exclude the influence of residue Zn in Ni_1–N–C-50, Ni_1–N–C-50-etch is also obtained by immersing Ni_1–N–C-50 in 1 M HCl for 2 hours to etch away most of Zn species (Table S2). The Ni_1–N–C-50-etch shows similar Ni content (1.4 %) and FE_{CO} (94 %) to Ni_1–N–C-50, further indicating the significance of single-atom Ni sites for CO_2RR rather than Zn (Figure S20 and Table S2). Moreover, Ni_1–N–C-50 shows the lowest Tafel slope (83 mV/decade), highest mass activity and the largest electrochemical active surface area (ECSA) among the Ni_1–N–C–X (X = 15, 50 and 100) series, indicating its faster reaction kinetics and better accessibility of active sites (Figure 3c, S21 and S22). In addition, the electrochemical impedance spectroscopy (EIS) analysis shows that the charge-transfer resistance (R_{ct}) of Ni_1–N–C-50 is also lower than Ni_1–N–C-15 under various potentials, suggesting the faster charge transfer of Ni_1–N–C-50 during CO_2 reduction (Figure S23–S25). Delightedly, the long-term operation measurement displays the outstanding
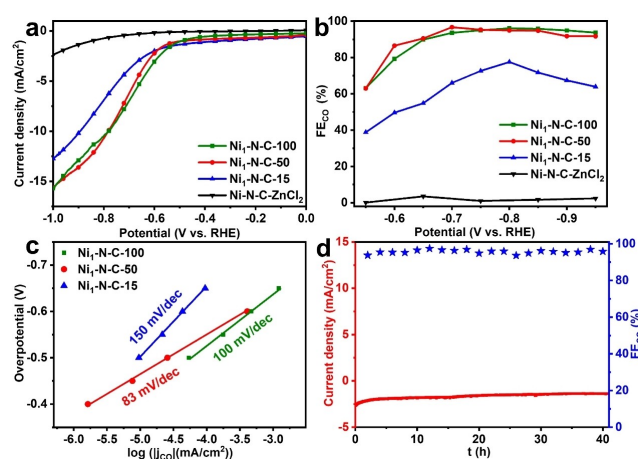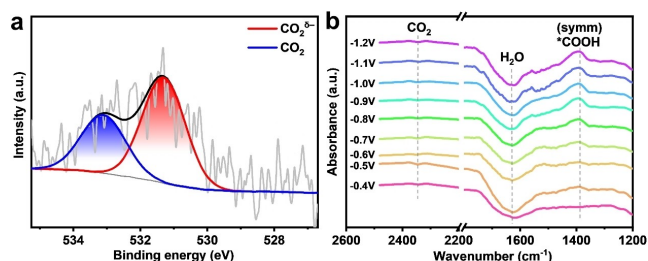
stability of Ni_1–N–C-50 with almost unchanged current density and FE_{CO} (Figure 3d).

To unveil the intrinsic mechanism for the enhanced catalytic performance of Ni_1–N–C-50, the CO_2 adsorption behavior has been investigated using near atmospheric pressure XPS (NAP-XPS) measurements. Both chemically adsorbed CO_2 ($CO_2^{\delta-}$) and physically adsorbed CO_2 can be observed in the O 1s spectra and Ni_1–N–C-50 exhibits a larger proportion of $CO_2^{\delta-}$ at 531.3 eV than Ni_1–N–C-15 (Figure 4a, S26 and S27).[17a,c] This manifests the better CO_2 adsorption and activation ability of Ni_1–N–C-50 due to its more abundant defective sites which is proved by Raman analysis (Figure S4). Moreover, in situ attenuated total reflection Fourier transform infrared (ATR-FTIR) spectroscopy measurements present that the *COOH signal (1396 cm^{-1}) for Ni_1–N–C-50 occurs at a lower potential (−0.5 V) than Ni_1–N–C-15 (−0.7 V) and the consumption of CO_2 is more significant for Ni_1–N–C-50 (Figure 4b and S28).[18] As the formation of *COOH is the rate-determining step for CO_2 electroreduction to CO, the results of FTIR spectra are reasonable and support the better performance of Ni_1–N–C-50.

To break the mass transfer limitation of CO_2 in the H-cell, the electrochemical performance of Ni_1–N–C-50 has been further evaluated in flow cell equipped with a gas diffusion electrode (GDE) (Figure 5a). The Ni_1–N–C-50 exhibits a high current response and achieves a high FE_{CO} above 95 % in the total current (j) range from 0.2 to 1.1 A/cm^2 (Figure 5b and S29). The j_{CO} reaches as high as 1.06 A/cm^2 with the FE_{CO} of 96 %, offering a broad future for industrial applications (Figure 5b). In stark contrast, the largest j and j_{CO} for Ni_1–N–C-furnace which can maintain the FE_{CO} above 90 % are 0.25 and 0.23 A/cm^2, respectively, much smaller than those of Ni_1–N–C-50, clearly reflecting the superiority of Ni_1–N–C-50 with mesoporous feature (Figure 5c). To further confirm the significance of the mesoporous structure, Ni_1–N–C-furnace-meso with abundant mesopores has also been deliberately prepared by conventional furnace pyrolysis of Ni-ZIF-8 (Figure S30 and S31). The largest j_{CO} of Ni_1–N–C-furnace-meso to maintain the FE_{CO} above 90 % reaches 0.39 A/cm^2, higher than Ni_1–N–C-furnace with only micropores (Figure 5c and S32). This clearly verifies the great contribution of the mesoporous structure for improved j_{CO}. In addition, Ni_1–N–C-50 also keeps a stable current density and FE_{CO} during

Figure 3. a) LSV curves and b) FE_{CO} of Ni–N–C–$ZnCl_2$ and Ni_1–N–C–X (X = 15, 50 and 100) in H-cell. c) Tafel plots of Ni_1–N–C–X (X = 15, 50 and 100). d) Durability test for Ni_1–N–C-50 in CO_2-saturated 0.5 M $KHCO_3$ at −0.7 V vs RHE.

Figure 4. a) Intensity changes of O 1s NAP XPS spectra induced by CO_2 adsorption on Ni_1–N–C-50. b) In situ ATR-FTIR spectra of Ni_1–N–C-50 during CO_2 reduction.
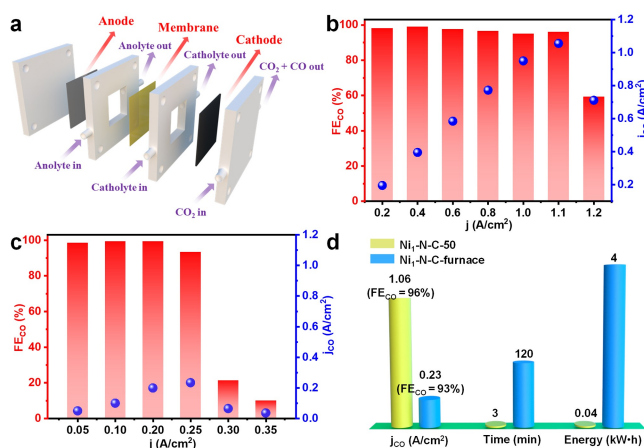
Figure 5. a) Schematic illustration of a flow cell with the gas diffusion electrode for CO_2 electroreduction. The values of FE_{CO} and j_{CO} of b) $Ni_1–N–C-50$ and c) $Ni_1–N–C$-furnace tested by chronopotentiometric measurements under various current densities. d) Comparison of j_{CO} (tested in the flow cell), time and energy consumption in the pyrolysis process between $Ni_1–N–C-50$ and $Ni_1–N–C$-furnace.

continuous electrolysis in flow cell (Figure S33). The results above unambiguously demonstrate that $Ni_1–N–C-50$ prepared by microwave-assisted strategy is much superior to $Ni_1–N–C$-furnace obtained via traditional electric heating from the aspects of both material synthesis (time and energy consumption) and catalytic performance (Figure 5d).

In view of the excellent performance of $Ni_1–N–C-50$ obtained by the microwave-assisted heating method, the adaptability of this heating method has been further investigated. Starting from different MOF precursors (Co-ZIF-8, Fe-ZIF-8 and Ni-PCN-222), a series of carbon-based SACs with various metal atoms have been successfully fabricated via such a microwave-assisted pyrolysis process (Figure S34–S38, Table S5). In addition to MOF precursors, such a microwave-assisted pyrolysis method is also successfully implemented in other organic precursors (such as the mixture of NiPc and ascorbic acid) (Figure S36, S37d and S38d, Table S5). More importantly, a large-scale synthesis of $Ni_1–N–C-50$ (~10 g) with Ni loading of 1.4 wt % is easily achieved within 3 min, illustrating the great potential of the microwave-assisted pyrolysis method for large-scale production of SACs (Figure S39 and S40, Table S2).

Conclusion

In summary, a rapid and general microwave-assisted heating approach has been developed to afford carbon-based SACs under the assistance of $ZnCl_2$ and KCl mixture. Compared with the conventional electric heating method, the microwave-assisted heating offers great advantages, including low cost, time saving and easy handling, making it highly promising for the large-scale industrial production of SACs. Specifically, the as-synthesized $Ni_1–N–C-50$ exhibits impressive performance reaching high j_{CO} (1.06 A/cm²) and FE_{CO} (96 %), far surpassing that of $Ni_1–N–C$-furnace (0.23 A cm^{-2}

with FE_{CO} of 93 %) obtained through traditional pyrolysis, in the electrochemical CO_2 reduction. Mechanism investigations reveal that the carbon defects and mesoporous structure of $Ni_1–N–C-50$ greatly improve CO_2 activation and mass transfer during catalysis, resulting in a high current density that preliminarily meets industrial requirements. This work develops a promising synthetic protocol toward the facile preparation of SACs and provides an excellent catalyst for electrocatalytic CO_2 reduction with the current density at industrial level.

Conflict of Interest

The authors declare no conflict of interest.

Data Availability Statement

The data that support the findings of this study are available from the corresponding author upon reasonable request.

Keywords: Single-atom catalysts · CO_2 reduction · metal–organic frameworks · electrocatalysis · microwave

[1] a) B. Qiao, A. Wang, X. Yang, L. F. Allard, Z. Jiang, Y. Cui, J. Liu, J. Li, T. Zhang, *Nat. Chem.* **2011**, *3*, 634–641; b) S. Ji, Y. Chen, X. Wang, Z. Zhang, D. Wang Y Li, *Chem. Rev.* **2020**, *120*, 11900–11955; c) J. Gu, C.-S. Hsu, L. Bai, H. Chen, X. Hu, *Science* **2019**, *364*, 1091–1094; d) Y. Zeng, J. Zhao, S. Wang, X. Ren, Y. Tan, Y.-R. Lu, S. Xi, J. Wang, F. Jaouen, X. Li, Y. Huang, T. Zhang, B. Liu, *J. Am. Chem. Soc.* **2023**, *145*, 15600–15610; e) Y. Wei, M. Zhang, R. Zou, Q. Xu, *Chem. Rev.* **2020**, *120*, 12089–12174; f) F. Xie, X. Cui, X. Zhi, D. Yao, B. Johannessen, T. Lin, J. Tang, T. B. F. Woodfield, L. Gu, S.-Z. Qiao, *Nat. Synth.* **2023**, *2*, 129–139; g) L. Han, H. Cheng, W. Liu, H. Li, P. Ou, R. Lin, H.-T. Wang, C.-W. Pao, A. R. Head, C.-H. Wang, X. Tong, C.-J. Sun, W.-F. Pong, J. Luo, J.-C. Zheng, H. L. Xin, *Nat. Mater.* **2022**, *21*, 681–688; h) Z.-H. Xue, D. Luan, H. Zhang, X. W. Lou, *Joule* **2022**, *6*, 92–133.

Angew. Chem. Int. Ed. **2024**, *63*, e202318338 (5 of 6)

© 2024 Wiley-VCH GmbH

[2] a) X. Wang, Y. Jia, X. Mao, D. Liu, W. He, J. Li, J. Liu, X. Yan, J. Chen, L. Song, A. Du, X. Yao, *Adv. Mater.* **2020**, *32*, 2000966; b) S. Liu, C. Li, M. J. Zachman, Y. Zeng, H. Yu, B. Li, M. Wang, J. Braaten, J. Liu, H. M. Meyer, M. Lucero, A. J. Kropf, E. E. Alp, Q. Gong, Q. Shi, Z. Feng, H. Xu, G. Wang, D. J. Myers, J. Xie, D. A. Cullen, S. Litster, G. Wu, *Nat. Energy* **2022**, *7*, 652–663; c) Y. Ren, R. Chang, X. Hu, J. Guo, G. Hao, A. Lu, *Chin. Chem. Lett.* **2023**, *34*, 108634; d) X. Rong, H.-J. Wang, X.-L. Lu, R. Si, T.-B. Lu, *Angew. Chem. Int. Ed.* **2020**, *59*, 1961–1965; *Angew. Chem.* **2020**, *132*, 1977–1981.

[3] a) S. Yuan, J. Zhang, L. Hu, J. Li, S. Li, Y. Gao, Q. Zhang, L. Gu, W. Yang, X. Feng, B. Wang, *Angew. Chem. Int. Ed.* **2021**, *60*, 21685–21690; *Angew. Chem.* **2021**, *133*, 21853–21858; b) Z. Jin, P. Li, Y. Meng, Z. Fang, D. Xiao, G. Yu, *Nat. Catal.* **2021**, *4*, 615–622; c) A. Guan, Y. Fan, S. Xi, H. Huang, Q. Zhang, N. Lyu, B. Wu, Y. Chen, Z. Liu, C. Yang, Y. Ji, M. Kan, L. Zhang, G. Zheng, *ACS Mater. Lett.* **2023**, *5*, 19–26; d) S.-Y. Tang, Y.-S. Wang, Y.-F. Yuan, Y.-Q. Ba, L.-Q. Wang, G.-P. Hao, A.-H. Lu, *New. Carbon Mater.* **2022**, *37*, 237–244; e) E. Zhang, L. Tao, J. An, J. Zhang, L. Meng, X. Zheng, Y. Wang, N. Li, S. Du, J. Zhang, D. Wang, Y. Li, *Angew. Chem. Int. Ed.* **2022**, *61*, e202117347; *Angew. Chem.* **2022**, *134*, e202117347.

[4] a) J.-R. Huang, X.-F. Qiu, Z.-H. Zhao, H.-L. Zhu, Y.-C. Liu, W. Shi, P.-Q. Liao, X.-M. Chen, *Angew. Chem. Int. Ed.* **2022**, *61*, e202210985; *Angew. Chem.* **2022**, *134*, e202210985; b) L. Jiao, J. Zhu, Y. Zhang, W. Yang, S. Zhou, A. Li, C. Xie, X. Zheng, W. Zhou, S.-H. Yu, H.-L. Jiang, *J. Am. Chem. Soc.* **2021**, *143*, 19417–19424.

[5] a) W. Y. Noh, J. Mun, Y. Lee, E. M. Kim, Y. K. Kim, K. Y. Kim, H. Y. Jeong, J. H. Lee, H.-K. Song, G. Lee, J. S. Lee, *ACS Catal.* **2022**, *12*, 7994–8006; b) G. M. Tomboc, T. Kim, S. Jung, H. J. Yoon, K. Lee, *Small* **2022**, *18*, 2105680.

[6] a) F. Kishimoto1, T. Yoshioka, R. Ishibashi, H. Yamada, K. Muraoka, H. Taniguchi, T. Wakihara, K. Takanabe, *Sci. Adv.* **2023**, *9*, eadi1744; b) X. Wu, Z. Wang, D. Zhang, Y. Qin, M. Wang, Y. Han, T. Zhan, B. Yang, S. Li, J. Lai, L. Wang, *Nat. Commun.* **2021**, *12*, 4018.

[7] a) S. Głowniak, B. Szczęśniak, J. Choma, M. Jaroniec, *Adv. Mater.* **2021**, *33*, 2103477; b) H. Qiao, M. T. Saray, X. Wang, S. Xu, G. Chen, Z. Huang, C. Chen, G. Zhong, Q. Dong, M. Hong, H. Xie, R. Shahbazian-Yassar, L. Hu, *ACS Nano* **2021**, *15*, 14928–14937; c) C. Jia, S. Li, Y. Zhao, R. K. Hocking, W. Ren, X. Chen, Z. Su, W. Yang, Y. Wang, S. Zheng, F. Pan, C. Zhao, *Adv. Funct. Mater.* **2021**, *31*, 2107072.

[8] a) Y. Lin, D. W. Baggett, J.-W. Kim, E. J. Siochi, J. W. Connell, *ACS Appl. Mater. Interfaces* **2011**, *3*, 1652–1664; b) H. Fei, J. Dong, C. Wan, Z. Zhao, X. Xu, Z. Lin, Y. Wang, H. Liu, K. Zang, J. Luo, S. Zhao, W. Hu, W. Yan, I. Shakir, Y. Huang, X. Duan, *Adv. Mater.* **2018**, *30*, 1802146.

[9] a) X. Li, L. Lin, T. Chen, S. Park, M. Bae, Y. Cho, J. Lee, W. Zhang, Y. Piao, G. Diao, *Langmuir* **2023**, *39*, 6914–6923; b) F. Bu, W. Chen, J. Gu, P. O. Agboola, N. F. Al-Khalli, I. Shakir, Y. Xu, *Chem. Sci.* **2018**, *9*, 7009–7016.

[10] a) H.-C. Zhou, J.-R. Long, O. M. Yaghi, *Chem. Rev.* **2012**, *112*, 673–674; b) H. Furukawa, K. E. Cordova, M. O'Keeffe, O. M. Yaghi, *Science* **2013**, *341*, 1230444; c) R. Lin, Z. Zhang, B. Chen, *Acc. Mater. Res.* **2021**, *54*, 3362–3376; d) L. Jiao, H.-L. Jiang, *Chem* **2019**, *5*, 786–804.

[11] a) M. Zhao, K. Yuan, Y. Wang, G. Li, J. Guo, L. Gu, W. Hu, H. Zhao, Z. Tang, *Nature* **2016**, *539*, 76–80; b) L. Jiao, H.-L. Jiang, *Chin. J. Catal.* **2023**, *45*, 1–5; c) H. Huang, K. Shen, F. Chen, Y. Li, *ACS Catal.* **2020**, *10*, 6579–6586; d) X. Zhao, Y. Wang, D.-S. Li, X. Bu, P. Feng, *Adv. Mater.* **2018**, *30*, 1705189.

[12] a) Z. Jiang, X. Liu, X.-Z. Liu, S. Huang, Y. Liu, Z.-C. Yao, Y. Zhang, Q.-H. Zhang, L. Gu, L.-R. Zheng, L. Li, J. Zhang, Y. Fan, T. Tang, Z. Zhuang, J.-S. Hu, *Nat. Commun.* **2023**, *14*, 1822; b) L. Jiao, W. Yang, G. Wan, R. Zhang, X. Zheng, H. Zhou, S.-H. Yu, H.-L. Jiang, *Angew. Chem. Int. Ed.* **2020**, *59*, 20589–20595; *Angew. Chem.* **2020**, *132*, 20770–20776; c) Y. Jia, Z. Xue, J. Yang, Q. Liu, J. Xian, Y. Zhong, Y. Sun, X. Zhang, Q. Liu, D. Yao, G. Li, *Angew. Chem. Int. Ed.* **2022**, *61*, e202110838; *Angew. Chem.* **2022**, *134*, e202110838; d) J. Shan, J. Liao, C. Ye, J. Dong, Y. Zheng, S. Z. Qiao, *Angew. Chem. Int. Ed.* **2022**, *61*, e202213412; *Angew. Chem.* **2022**, *134*, e202213412; e) G. Chen, R. Lu, C. Li, J. Yu, X. Li, L. Ni, Q. Zhang, G. Zhu, S. Liu, J. Zhang, U. I. Kramm, Y. Zhao, G. Wu, J. Xie, X. Feng, *Adv. Mater.* **2023**, *35*, 2300907; f) Y. Zhang, L. Jiao, W. Yang, C. Xie, H.-L. Jiang, *Angew. Chem. Int. Ed.* **2021**, *60*, 7607–7611; *Angew. Chem.* **2021**, *133*, 7685–7689; g) C. Wen, F. Mao, Y. Liu, X. Zhang, H. Fu, L. Zheng, P. Liu, H. Yang, *ACS Catal.* **2020**, *10*, 1086–1093.

[13] C. Chen, M. R. Alalouni, X. Dong, Z. Cao, Q. Cheng, L. Zheng, L. Meng, C. Guan, L. Liu, E. Abou-Hamad, J. Wang, Z. Shi, K.-W. Huang, L. Cavallo, Y. Han, *J. Am. Chem. Soc.* **2021**, *143*, 7144–7153.

[14] a) S. M. Nyambura, C. Li, H. Li, J. Xu, J. Wang, X. Zhu, X. Feng, X. Li, G. V. Bertrand, J. N. Ndumia, B. L. F. Chin, *Fuel* **2023**, *352*, 129093; b) Y. Cheng, B. Li, Y. Huang, Y. Wang, J. Chen, D. Wei, Y. Feng, D. Jia, Y. Zhou, *Appl. Surf. Sci.* **2018**, *439*, 712–723.

[15] a) L.-B. Jiang, A.-H. Meng, Q.-Y. Zhang, *Acta Phys. Chim. Sin.* **2006**, *22*, 131–134; b) I. Bilecka, M. Niederberger, *Nanoscale* **2010**, *2*, 1358–1374; c) N. Yoshikawa, S. Mikoshiba, T. Sumi, S. Taniguchi, *Chem. Eng. Process.* **2017**, *115*, 56–62.

[16] L.-L. Ling, L. Jiao, X. Liu, Y. Dong, W. Yang, H. Zhang, B. Ye, J. Chen, H.-L. Jiang, *Adv. Mater.* **2022**, *34*, 2205933.

[17] a) H.-B. Yang, S.-F. Hung, S. Liu, K. Yuan, S. Miao, L. Zhang, X. Huang, H.-Y. Wang, W. Cai, R. Chen, J. Gao, X. Yang, W. Chen, Y. Huang, H.-M. Chen, C.-M. Li, T. Zhang, B. Liu, *Nat. Energy* **2018**, *3*, 140–147; b) X.-M. Liang, H.-J. Wang, C. Zhang, D.-C. Zhong, T.-B. Lu, *Appl. Catal. B* **2023**, *322*, 122073; c) B. Eren, R. S. Weatherup, N. Liakakos, G. A. Somorjai, M. Salmeron, *J. Am. Chem. Soc.* **2016**, *138*, 8207–8211.

[18] a) Y.-R. Wang, H.-M. Ding, X.-Y. Ma, M. Liu, Y.-L. Yang, Y. Chen, S.-L. Li, Y.-Q. Lan, *Angew. Chem. Int. Ed.* **2022**, *61*, e202114648; *Angew. Chem.* **2022**, *134*, e202114648; b) J.-D. Yi, R. Xie, Z.-L. Xie, G.-L. Chai, T.-F. Liu, R.-P. Chen, Y.-B. Huang, R. Cao, *Angew. Chem. Int. Ed.* **2020**, *59*, 23641–23648; *Angew. Chem.* **2020**, *132*, 23849–23856.